



# Analysis of Thunderstorms Producing Terrestrial Gamma Ray Flashes With the Meteosat Second Generation

A. Ursi<sup>1</sup> , M. Marisaldi<sup>2,3</sup> , S. Dietrich<sup>4</sup> , M. Tavani<sup>1,5</sup> , A. Tiberia<sup>4,6</sup> , and F. Porcu<sup>7</sup> 

<sup>1</sup>INAF-IAPS, National Institute for Astrophysics, Rome, Italy, <sup>2</sup>Birkeland Centre for Space Science, University of Bergen, Bergen, Norway, <sup>3</sup>INAF-Osservatorio di Astrofisica e Scienza dello Spazio di Bologna (OAS), National Institute for Astrophysics, Bologna, Italy, <sup>4</sup>ISAC-CNR, Institute for Atmospheric Science and Climate, Rome, Italy, <sup>5</sup>Dipartimento di Fisica, Università di Roma “Tor Vergata”, Rome, Italy, <sup>6</sup>Dipartimento di Fisica e Scienze della Terra, University of Ferrara, Ferrara, Italy, <sup>7</sup>Department of Physics and Astronomy, University of Bologna, Bologna, Italy

## Key Points:

- Thunderstorms associated to TGF production mainly occur at low latitudes, over land regions, and in the afternoon
- Most of the thunderstorms found producing TGFs exhibit a wide range of cloud top temperatures and cloud extensions, but high cloud top heights
- TGFs tend to occur within  $\pm 5$  min from the peak lightning activity of the associated thunderstorm

## Supporting Information:

- Supporting Information S1
- Data Set S1

## Correspondence to:

A. Ursi,  
alessandro.ursi@inaf.it

## Citation:

Ursi, A., Marisaldi, M., Dietrich, S., Tavani, M., Tiberia, A., & Porcu, F. (2019). Analysis of thunderstorms producing Terrestrial Gamma ray Flashes with the Meteosat Second Generation. *Journal of Geophysical Research: Atmospheres*, 124, 12,667–12,682. <https://doi.org/10.1029/2018JD030149>

Received 11 JAN 2019

Accepted 5 JUN 2019

Accepted article online 8 OCT 2019

Published online 8 DEC 2019

**Abstract** Up to now, only few works focused on the meteorological context leading to the production of Terrestrial Gamma ray Flashes (TGFs). In this study, we carry out, for the first time, an analysis on large scale of the meteorological scenario linked to 278 TGFs detected by RHESSI, AGILE, and Fermi, by using the Meteosat Second Generation geostationary satellites. These satellites are useful as they continuously monitor the same geographic region in time, allowing investigations on thunderstorms' development; moreover, they are endowed with channels and products that provide information about the meteorological context under analysis, such as the cloud top temperature and altitude, the cloud extension, the drop effective radius and the cloud phase. Our work confirms what previously found in other studies about the TGF-associated thunderstorms, by using a different approach and by using for the first time the Meteosat satellites: we find TGFs mostly linked to the development phase of deep convective thunderstorm systems, exhibiting typical characteristics of tropical storms, and providing a first picture on large scale of the TGF-associated thunderstorm systems.

## 1. Introduction

Terrestrial Gamma ray Flashes (TGFs) consist of submillisecond gamma ray emissions with energies up to tens of mega-electron volts, occurring during thunderstorms and associated with lightning activity. Discovered by the Compton Gamma-Ray Observatory in 1994 (Fishman et al., 1994), they have been later largely detected by satellites devoted to high-energy astrophysics: the Reuven Ramaty High-Energy Spectroscopic Imager (RHESSI; Grefenstette et al., 2009; Smith et al., 2005, 2010), the Astrorivelatore Gamma ad Immagini LEggero (AGILE; Marisaldi et al., 2010, 2015), and the Fermi Space Telescope (Briggs et al., 2010, 2013; Roberts et al., 2018). Recently, TGFs have been found in the Satellite per Astronomia X (Beppo-SAX) satellite data archive as well (Ursi, Guidorzi, et al., 2017).

TGFs are thought to consist of Bremsstrahlung photons produced by relativistic electrons accelerated in thunderstorm electric fields and abruptly braked in the atmosphere: several models have been proposed to describe in detail this process (Celestin et al., 2012; Carlson et al., 2010; Dwyer, 2008, 2012; Dwyer et al., 2003; Gurevich et al., 1992; Liu & Dwyer, 2013; Moss et al., 2006; Pasko, 2014; Wilson, 1924, 1925).

Despite the atmospheric nature of TGFs, only few studies have been carried out concerning the meteorological context associated to these events. The typical geographic, seasonal, and local time distribution of TGFs follows that of tropical storms (Splitt et al., 2010), mostly concentrating within the near-equatorial trough of the Intertropical Convergence Zone (ITCZ): however, the different production regions and local time variations appear not to affect the intrinsic TGF characteristics, as shown by Grefenstette et al. (2009) on RHESSI TGFs.

TGFs have been detected coming from a wide range of altitudes, by using high-energy detectors placed onboard satellites, airborne and on-ground gamma ray and particle detectors. Dwyer and Smith (2005) first performed Monte Carlo simulations to estimate the production altitude required for TGFs to survive to spacecraft altitudes, ending up with heights between 15 and 20 km. Such result was later confirmed by Splitt et al. (2010) using RHESSI data, whereas Cummer et al. (2014) presented two events detected by the Gamma-ray Burst Monitor, whose source region was reconstructed at 11- to 12-km altitude in the interior of

the thunderstorm charge layers. Nevertheless, TGFs have been detected even at lower altitudes, as showed by Shao et al. (2010) and Xu et al. (2012), as well as by detectors placed onboard aircraft, such as the Airborne Detection for Energetic Lightning Emission (Smith et al., 2011) and at ground level (Abbasi et al., 2018; Bowers et al., 2017, 2018; Dwyer et al., 2012; Hare et al., 2016; Tran et al., 2015).

A fraction of detected TGFs are usually found simultaneous with lightning-generated radioatmospherics (sferics), detected on-ground by lightning location networks within hundreds of microseconds (Connaughton et al., 2013; Inan et al., 1996; Marisaldi et al., 2015; Mezentsev et al., 2016). This further established the deep correlation between lightning discharges and TGFs. Although the detailed relationship between the two processes is still not clear. TGFs seem to be more likely associated to particular types of lightning discharges: Shao et al. (2010) and Cummer et al. (2014, 2015) found out that TGFs tend to be produced at the developing stages of relatively long ( $\sim 2$  km) upward propagating IntraCloud leaders, with high upward velocity ( $\sim 1.0 \times 10^6$  m/s), suggesting the possibility of a more likely relation with strong in-cloud electric fields and large potential differences. The lightning discharge – TGF ratio appear to be affected by geographic discrepancies (taking into consideration the relative geographic lightning detection efficiency), with a lack of events in the South American zone (Fuschino et al., 2011).

Smith et al. (2010) studied the variation of lightning discharge rate during single storms associated to TGF production and found that the  $\pm 20$ -min interval about the TGF time mostly included the decreasing stages of the lightning rate. On the contrary, Ursi, Sanò, et al. (2017) showed a case study over Africa, for which a TGF was taking place during the cooling phase of the thunderstorm and the increasing stages of the lightning rate.

In the light of the few studies carried out up to now, thunderstorms that produce TGFs seem not to exhibit particular characteristics with respect to storms not associated to TGFs. Splitt et al. (2010) found RHESSI events occurring during storms whose extension vary from single storms to large mesoscale convective systems. The same result was obtained by Chronis et al. (2016), who analyzed 24 Fermi TGFs over Florida, whose associated storms exhibited a wide range of intensities, from relatively weak systems to deeper convective ones. Fabró et al. (2015) carried out an extensive study by using GOES geostationary satellites, on a sample of hundreds of AGILE and RHESSI TGFs over South America, confirming the seasonal and local time distribution of TGFs and finding them occurring under rare conditions of flash rate, but under a wide range of Convective Available Potential Energy and cloud extensions. Barnes et al. (2015) retrieved information on the microphysics of thunderstorms from the Tropical Rainfall Measurement Mission, finding out a higher content of hydrometeor, cloud and precipitation water, and cloud and precipitation ice at higher altitudes for storms found producing TGFs, with respect to storms with no associated TGF. Roberts et al. (2017) compared TGFs produced during tropical storms, whose producing cell can be randomly placed inside the convective system, to TGFs produced during typhoons and hurricanes, whose producing region is usually placed in the outer rainband, where a highest lightning rate is present. Moreover, the largest fraction of their events seems to take place during the strengthening phase of the tropical storm system.

## 2. Data Sample, Products, and Methods

### 2.1. TGF Sample and Satellites

In more than 15 years activity, RHESSI, AGILE, and Fermi contributed to build up a global database of thousands of TGFs, fundamental to investigate the phenomenology of these events. From that database, we selected all events occurring within the  $60^\circ\text{W}$  to  $60^\circ\text{E}$ ,  $60^\circ\text{S}$  to  $60^\circ\text{N}$  geographic region, found in close time association with a World Wide Lightning Location Network (WWLLN) sferic (within  $200 \mu\text{s}$  for Fermi and within  $500 \mu\text{s}$  for RHESSI and AGILE), in order to achieve the most reliable localization of the corresponding source regions ( $< 20$  km, according to the WWLLN spatial resolution; Rodger et al., 2009).

We ended up with a sample of 278 TGFs shown in Figure 1. The selected TGF sample covers a period from 2003 to 2015, spanned over a wide range of latitudes. In particular, the 65 RHESSI TGFs with associated sferic were provided by Gjesteland et al. (2012) and refer to a period from 2003 to 2013, ranging within  $\pm 38^\circ$  latitude; the 22 AGILE TGFs with associated sferic refer to the 3-month period, from March 2015 to June 2015, during the enhanced TGF detection phase of the MiniCALorimeter instrument, as illustrated in Marisaldi et al. (2015), and range within  $\pm 2.5^\circ$  latitude (TGF catalog available on <https://www.ssdsc.asi.it/mcaletgfcatalog/>); the Fermi TGFs with associated sferic are taken from the public Fermi Gamma-ray Burst Monitor TGF catalog (available on <https://fermi.gsfc.nasa.gov/ssc/data/access/gbm/tgf/>), recently published by Roberts et al. (2018), and refer to a period from 2008 to 2015, ranging within  $\pm 26^\circ$  latitude.

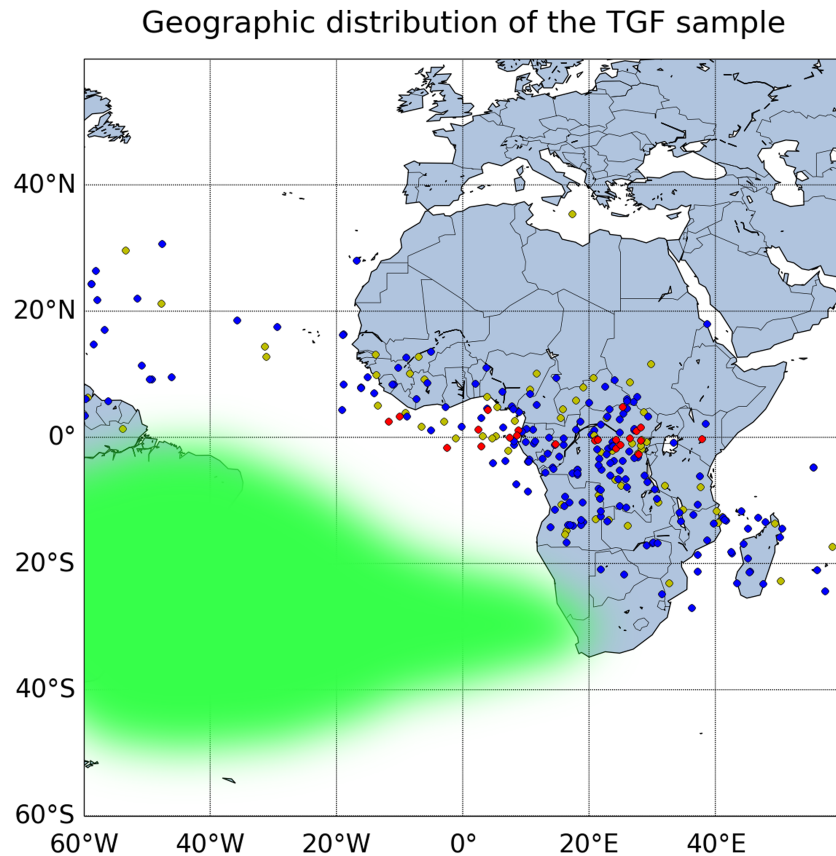


**Figure 1.** The TGF sample used for the present work: 65 TGFs detected by Reuven Ramaty High-Energy Spectroscopic Imager (green dots), 22 TGFs detected by Astrorivelatore Gamma ad Immagini LEggero (red dots), and 191 TGFs detected by Fermi (blue dots), covered by the Meteosat Second Generation geostationary satellites. The green shaded region corresponds to the South Atlantic Anomaly, where the high concentration of charged particles prevents the detection of TGFs. TGFs = Terrestrial Gamma ray Flashes.

The obtained sample of 278 events with associated sferic is quite small with respect to the total TGF database of the three missions, representing only a small fraction of the respective full TGF databases acquired by each satellite in the same period, as shown in Figure 2. Furthermore, the selected subsample of WWLLN-associated TGFs within the 60°W to 60°E region turns out to be much smaller than the fraction of WWLLN-associated TGFs found in other geographic regions: this is justified by the lower detection efficiency of the WWLLN in the African continent (Hutchins et al., 2012).

## 2.2. Meteorological Satellites and Data

The information retrieved to study the meteorological context associated to our TGF sample was obtained by using geostationary satellites. The strongest point of the geostationary orbit is the continuous monitoring of a same Earth full disk surface: this allows to investigate the meteorological evolution of a given geographic region in time, though with a coarse time resolution given by the delivery of data, usually ranging from 15 to 60 min, depending on satellite and period.

For our analysis, we made use of the first three Meteosat Second Generation (MSG) geostationary satellites, Meteosat-8 (MSG1), Meteosat-9 (MSG2), and Meteosat-10 (MSG3), a series of satellites operated by the European organization for the exploitation of METeorological SATellites (EUMETSAT), whose data are delivered at the rate of one Earth full-disk scan every 15 min (Schmetz et al., 2002). The nominal orbit of these satellites is the geostationary orbit centered at (0°E, 0°N), devoted to the scan of the Earth full-disk between 60°W to 60°E and 60°S to 60°N: whenever a successive satellite is launched, it is delivered into this orbit, displacing and recentering the previous one at a different orbital position, still serving as backup. We focused our analysis on the 60°W to 60°E longitude range, whose meteorological data are always provided by the MSG program throughout the time period under analysis.

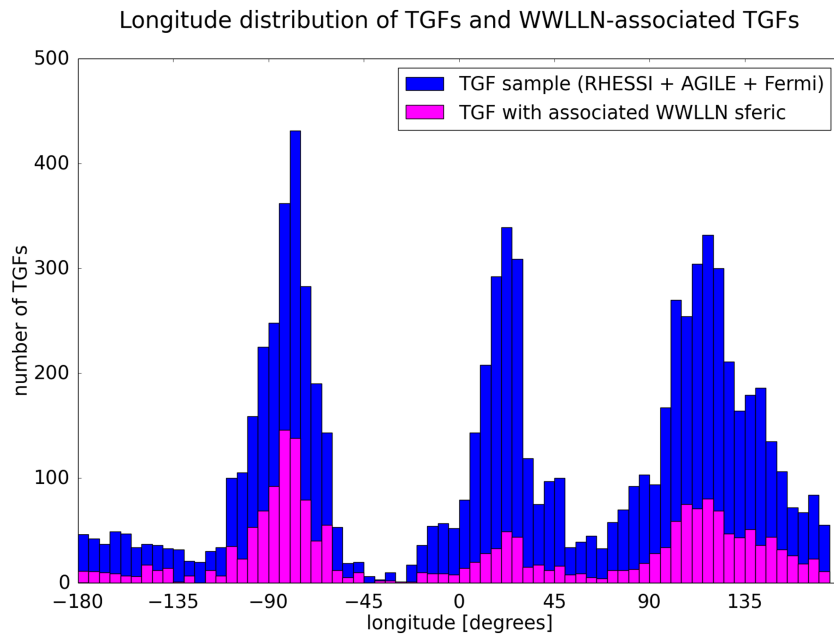


**Figure 2.** Longitude distribution of all RHESSI, AGILE, and Fermi TGFs (blue), detected in the period of interest, and the fraction of those events found in close time association with a WWLLN sferic (magenta). RHESSI = Reuven Ramaty High-Energy Spectroscopic Imager; AGILE = Astrorivelatore Gamma ad Immagini LEggero; WWLLN = World Wide Lightning Location Network; TGFs = Terrestrial Gamma ray Flashes.

As products of meteorological interest, we made use of the data acquired by the Spinning Enhanced Visible and InfraRed Imager (SEVIRI) instrument, available onboard each satellite of the MSG series and providing data in both thermal infrared and visible wavelengths. In particular, the High Rate SEVIRI Level 1.5 Image Data provide a 3 km (1 km for the High-Resolution Visible channel) spatial resolution at (0°E, 0°N), and decreasing with increasing distance from the subsatellite point. We considered the infrared 10.8 μm and water vapor 6.2 μm channels: the first one provides direct information on the cloud top temperature (CTT; Mecikalski et al., 2010a, 2010b) and, with the second one, allows for the reconstruction of the Global Convective Diagnostics (GCD) parameter, useful for the identification of convection in atmosphere (Ackerman, 1996; Mosher, 2001). From the infrared temperature it is possible to perform an estimate of the cloud size, that we call cloud top coverage (CTC), by computing the storm total surface area with temperatures below -70 °C, taking into consideration the 3-km horizontal spatial resolution of the SEVIRI channels and its variation with respect to the distance from the subsatellite point. Computing the rate at which the CTT varies in time provides the cooling rate (CR) of the thunderstorm, defined as the derivative of temperature with respect to time. Moreover, we considered also the cloud top height (CTH) parameter, a EUMETSAT product providing information on the cloud altitude, with spatial resolution of 4 km at (0°E, 0°N), and vertical resolution of 320 m (from 960 to 16,000 m; information on this product can be found on <https://www.eumetsat.int/>). This product is disseminated every 15 min repeat cycle only since June 2011: as a consequence, CTH is available for only 198 TGFs out of the total sample, not providing information on a fraction of events detected between 2003 and 2011.

MSG data are delivered to the community every 15 min: as a consequence, for each TGF-associated sferic occurring at  $t_{\text{TGF}}$ , we may have a delay up to  $\pm 7.5$  min between the event and the associated meteorological data. Moreover, Meteosat satellites do not acquire data instantaneously, but scanning the whole Earth disk from 60°S to 60°N in a total time of about 12 min, in fact observing different latitudes at different times: this introduces a delay between the nominal time at which the MSG data packet is delivered  $t_{\text{MSG}}$  and the true time  $t_{\text{eff}}$  of observation of a certain geographic region at latitude  $L$ , roughly estimated as  $t_{\text{eff}} = t_{\text{MSG}} - \frac{L+60}{10}$ . This time difference between the TGF-associated sferic and MSG data  $\Delta t = |t_{\text{TGF}} - t_{\text{MSG}}|$  may play a role when analyzing the meteorological context, making the meteorological data less reliable when the  $\Delta t$  is large. For this reason, we considered three classes of data,  $\Delta t \leq 1.0$  min,  $1.0 \text{ min} < \Delta t \leq 3.0$  min, and

**Table 1**  
*TGF Parameters and Meteorological Parameters Adopted for the Analysis of the TGF Sample*

TGF parameters name	Description
Detecting satellite	RHESSI
	AGILE
	Fermi
Time delay	$\Delta t \leq 1.0$ min
	$1.0 \text{ min} < \Delta t \leq 3.0$ min
	$3.0 \text{ min} < \Delta t \leq 7.5$ min
Local time	morning, 04:00–12:00
	afternoon, 12:00–20:00
	night, 20:00–04:00
Geographic latitude	$10^\circ\text{S}$ to $10^\circ\text{N}$
	$20\text{--}10^\circ\text{S}$ and $10\text{--}20^\circ\text{N}$
	$40\text{--}20^\circ\text{S}$ and $20\text{--}40^\circ\text{N}$
Geographic region	land, $>1^\circ$ from coast
	coast, within $1^\circ$ from coast
	ocean, $>1^\circ$ from coast

$3.0 \text{ min} < \Delta t \leq 7.5$  min, the class being another parameter associated to our TGFs and describing the quality of the observation.

Another interesting information that can be obtained with the SEVIRI instrument is represented by the cloud drop effective radius (ER) and the cloud phase (CP), which provide the identification of the hydrometeor phase of the cloud under analysis and the percentage of ice content: these parameters give an insight on the cloud, allowing to discriminate between water clouds and ice clouds; in particular, the CP parameter allows to distinguish single-layer water clouds, from single layer or two layer with high concentration of ice particles. ER and CP can be obtained from the EUMETSAT Cloud Optimal Analysis product that makes use of an optimal estimation method and of all the SEVIRI spectral measurements. This product is disseminated at hourly frequencies since June 2013 and is therefore available only for 33 TGFs of our sample.

Finally, it is also interesting to characterize the convective systems under analysis by means of the lightning discharges produced, which we call lightning flash rate (LFR) parameter: in order to do that, we made use of WWLLN data, whose time resolution of microseconds allows to better investigate the meteorological scenario on smaller timescales, closer to the TGF production stages.

### 2.3. Methods and Analysis

First, each TGF was classified by considering parameters that could provide a picture of our sample: the detecting spacecraft (i.e., RHESSI, AGILE, or Fermi), the delay between TGF and MSG data (i.e.,  $\Delta t$ ), the local time interval at which the event occurs (i.e., morning 04:00–12:00, afternoon 12:00–20:00, or night 20:00–04:00), the geographic latitude band (i.e., within  $10^\circ$ , between  $10^\circ$  and  $20^\circ$ , or between  $20^\circ$  and  $40^\circ$ , in absolute value), and the geographic region where it was detected (i.e., land, ocean, or coast, defined as events occurring at distances  $<1^\circ$ , within  $\pm 1^\circ$ , and  $>1^\circ$  from the coastal contours, respectively). Physical intrinsic parameters, such as the TGF duration, fluence, photon energy, or the delay with respect to the associated sferic have been neglected, as they strongly depend on the detection capabilities and sensitivity of the detectors, not providing a homogeneous sample for analysis purposes.

A comprehensive summary of all the adopted TGF and meteorological parameters is given in Table 1. An example of a TGF, detected by AGILE and classified by means of its meteorological parameters, is shown in Figure 3: the corresponding TGF and meteorological parameters are presented in Tables 2a, 2b, and 3a–3c.

For each TGF, we retrieved the meteorological parameters of the associated storm, on different time intervals, spatial areas, and time resolution. The CTT and GCD parameters are taken as the lowest values evaluated in a time interval of  $\pm 100$  min about the TGF time, and within a  $0.25^\circ$  (corresponding to about 30 km) radius circle around each sferic position: such value allows to exploit the localization resolution of

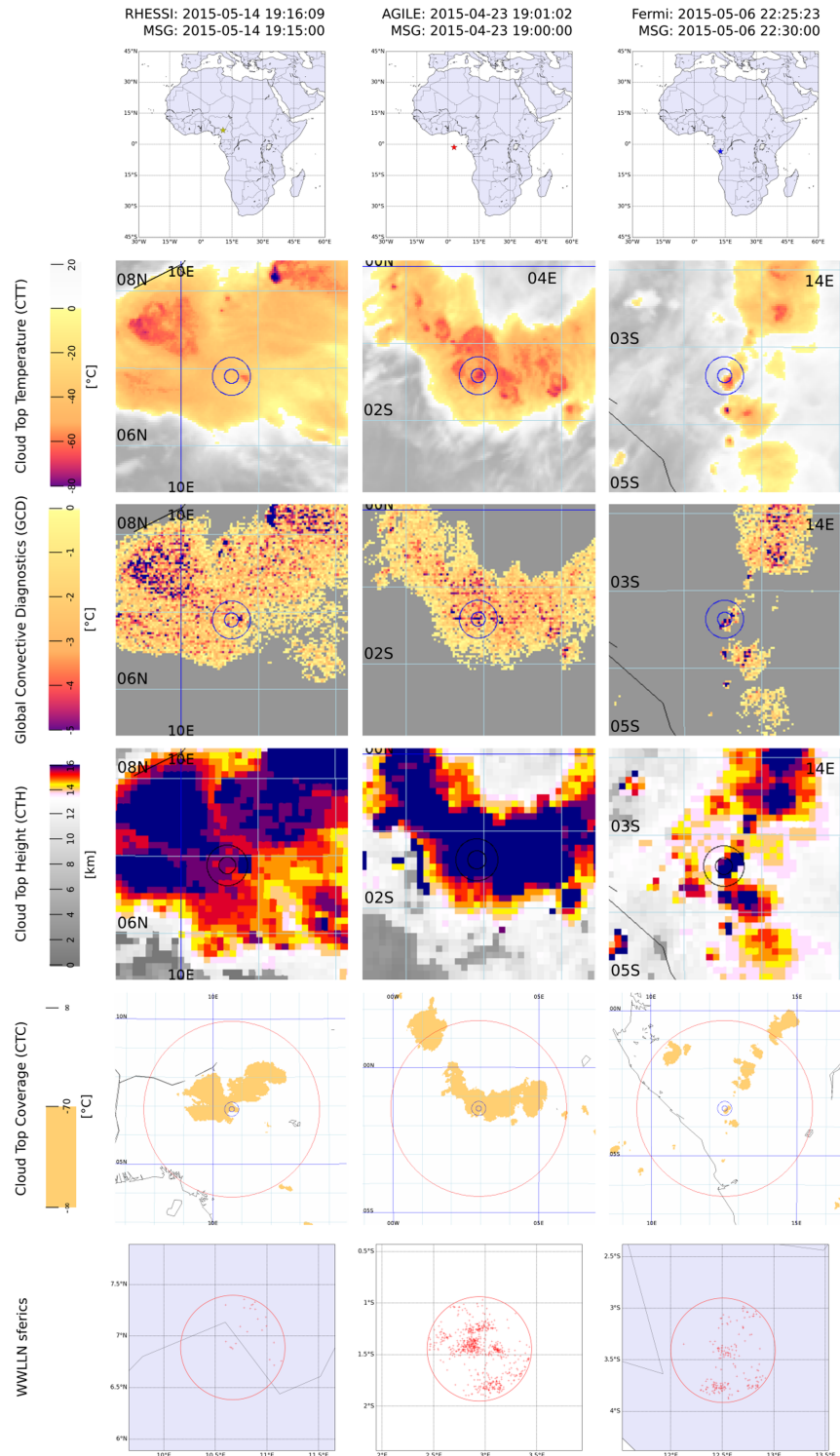


**Figure 3.** Example of the meteorological products used for the analysis, referred to three TGFs detected by RHESSI (first columns), AGILE (second column), and Fermi (third column). The CTT, GCD, and CTH are analyzed within a  $0.25^\circ$  radius circle from the subsatellite point. The CTC is evaluated within a larger  $3.00^\circ$  radius area, in order to contain the whole, or most of the associated storm. These parameters are evaluated on a  $\pm 100$ -min time interval around the TGF time (here is shown only the central time bin). The lightning flash rate is analyzed within a  $0.25^\circ$  radius circle around the TGF-associated WWLLN sferic and evaluated on a  $\pm 40$  min time interval. RHESSI = Reuven Ramaty High-Energy Spectroscopic Imager; AGILE = Astrorivelatore Gamma ad Immagini LEggero; WWLLN = World Wide Lightning Location Network; TGFs = Terrestrial Gamma ray Flashes.

**Table 2a**  
*Example of TGF Parameters Associated to a TGF Detected by AGILE*

Meteo parameters name	Description	Area	Time interval	Time bin
CTT	minimum $T_{10.8\mu\text{m}}$	0.25°	$\pm 100$ min	15 min
GCD	minimum $T_{10.8\mu\text{m}} - T_{6.2\mu\text{m}}$	0.25°	$\pm 100$ min	15 min
CTH	maximum height	0.25°	$\pm 100$ min	15 min
CTC	$\sum \text{CTT} \leq -70^\circ$	3.00°	$\pm 100$ min	15 min
CR	$\text{CTT}_{\text{fin}} - \text{CTT}_{\text{in}} / 100$ min	0.25°	—	60 min
ER	median ER	0.25°	—	60 min
CP	median CP	0.25°	—	60 min
LFR	WWLLN lightning flash rate	0.25°	$\pm 40$ min	1 min, 5 min

WWLLN sferics ( $\sim 20$  km), in order to study the closest storm regions producing the detected TGFs. The CTH parameter is taken as the highest value evaluated in a 0.25° radius circle and on a  $\pm 100$ -min time interval as well. We choose to select those values, in order to better highlight the most extreme conditions present in the geographic area under consideration. The CTC parameter was evaluated by integrating all data with  $\text{CTT} < -70^\circ$  within a larger area of 3° radius, corresponding to  $\sim 350$  km, in order to contain the whole storm. The CTT, GCD, CTH, and CTC parameters are all evaluated at steps of 15 min, given by the Meteosat time resolution. On the other hand, the CR is estimated by considering the temperature rate of change throughout the entire cooling process, in the 60 min before the TGF and in the 60 min following the TGF.

ER and CP parameters are estimated as the median value within the 0.25° radius circle around the TGF position. The hourly time resolution at which ER and CP product are disseminated prevents any study on the time evolution of these parameters; as a consequence, ER and CP are only evaluated at the single time interval within 7.5 min from the TGF time (i.e., between hh:52:30 and hh+1:07:30) and no characterization of their development in time is carried out.

Finally, the LFR parameter was considered only for a time interval of  $\pm 40$  min around the TGF time, at time steps of 5 min. An example of the meteorological products evaluated for this analysis is given in Figure 3, where the CTT, GCD, CTH, and CTC are presented, related to three TGFs of our sample, detected by RHESSI, AGILE, and Fermi, respectively.

### 3. Results and Discussion

#### 3.1. TGF Parameters

First of all, we investigated the  $\Delta t$  parameter, in order to assess whether the time offset between the MSG data and the TGF plays a role in describing the meteorological scenario. The general trends of the total distributions of the meteorological parameters are generally followed by each class of  $\Delta t$ , allowing us to treat all Meteosat data as reliable and consistent with the TGF time of occurrence. As a consequence, for the rest of the study, we neglected the  $\Delta t$  parameter.

We filled in a database in which each event is characterized by its TGF parameters and the meteorological parameters of the associated storm. We built up cumulative distributions of the main parameters for the

**Table 2b**  
*Example of TGF Parameters Associated to a TGF Detected by AGILE*

TGF150423	
Time	2015-04-23 19:01:02.116 (UT)
Detecting satellite	AGILE
Time delay	$\Delta t = 1$ min
Local time	afternoon
Geographic latitude	1.43°S
Geographic region	ocean

**Table 3a**

Example of meteorological parameters associated to the TGF detected by AGILE on 23 April 2015 19:01:02 (UT), also presented in Tables 2a and 2b

Parameters	Values										
$t - t_{\text{MSG}}$ (min)	-100	...	-45	-30	-15	0	+15	+30	+45	...	+100
CTT ( $^{\circ}\text{C}$ )	-78.65	...	-83.22	-80.06	-83.22	-81.92	-82.57	-84.56	-82.57	...	-81.74
GCD ( $^{\circ}\text{C}$ )	-1.59	...	-3.09	-3.02	-3.09	-2.9	-3.09	-3.09	-3.45	...	-3.17
CTH (km)	$\geq 14.4$	...	$\geq 15.04$	$\geq 15.04$	$\geq 15.04$	$\geq 15.04$	$\geq 15.04$	$\geq 15.04$	$\geq 15.04$	...	$\geq 15.04$
CTC ( $\text{km}^2$ )	62,055	...	70,589	74,781	75,466	80,428	83,594	84,193	84,706	...	84,613
ER ( $\mu\text{m}$ )	...	...	...	...	...	20.2	...	...	...	...	...
CP	...	...	...	...	...	two-layer ice cloud	...	...	...	...	...

TGF sample as a whole, in order to study the general features of our TGF population. In Figure 4, distributions for the TGF properties of our sample are presented. The TGF events acquired by RHESSI, AGILE, and Fermi do not represent a homogenous sample, for what concerns both the detection periods and the covered geographic regions: these satellites house detectors with different energy ranges and sensitivities, orbit at different inclinations collecting different surface exposures, and acquired the related TGF subsamples during only partially overlapping time periods. As a consequence, the cumulative distributions of the TGF parameters only serve to describe the adopted sample and do not constitute a general characterization of the TGF phenomenon: for the analysis, we kept separated the three satellites TGF subsample contributions.

The yearly distributions show the different and nonuniform periods considered for each spacecraft, partially overlapping and not covering an integer number of years: this affected the related monthly distributions, although they clearly show the general trend peaking in the spring and autumn, due to the ITCZ crossing the equatorial strip. The local time distributions, which can be considered the only actual homogeneous distributions, due to the large number of days considered in the analysis ( $\sim 250$  days), clearly follow the diurnal pattern of lightning flashes, preferring afternoons.

The geographic distributions are affected by the different surfaces covered by the three satellites, with most of TGFs occurring within the  $10^{\circ}\text{S}$  to  $10^{\circ}\text{N}$  latitude range, common to all spacecraft, as already displayed in Figure 1. Nevertheless, they globally follow the typical storm distribution, with the greatest fraction of events occurring over land, corresponding to the African continent: the lack of data over the Atlantic Ocean can be ascribed to the lower lightning occurrence, to the lower WWLLN sensitivity, but also to the presence of the South Atlantic Anomaly, where detectors are usually switched off due to the presence of a high charged particle background that prevents detections. The longitude distributions exhibit the typical sharp LFR gradient at  $30^{\circ}\text{E}$ , given by the orographic structure of the eastern edge of the Congo basin.

### 3.2. TGF-Associated Storms Meteorological Parameters

We start cross correlating the TGF parameters of our sample with meteorological data associated to the producing storm. We focus on the scenario at the time at which our TGFs occurred, by studying the CTT, GCD, CTH, and CTC parameters provided by the closest in time available MSG data, related to the TGF-associated storm, as well as the LFR parameter, evaluated on a time interval of  $\pm 2.5$  min around each TGF. Distributions of all parameters are shown in Figure 5, for all TGFs of our sample, by evaluating MSG data within  $0.25^{\circ}$  around each TGF-associated spheric position: the plots show the distributions evaluated for the total TGF population, considered as a unique homogenous sample. On the other hand, Figure 6 shows the same meteorological parameters, evaluated with respect to the different TGF parameters of the sample (i.e., detecting satellite, time delay, local time, spheric latitude, and geographic region): these distributions are displayed

**Table 3b**

Example of meteorological parameters associated to the TGF detected by AGILE on 23 April 2015 19:01:02 (UT), also presented in Tables 2a and 2b

Parameters	Values	
$t - t_{\text{MSG}}$ (min)	$t_{\text{TGF}} - 60, t_{\text{TGF}}$	$t_{\text{TGF}}, t_{\text{TGF}} + 60$
CR ( $^{\circ}\text{C}/\text{min}$ )	-0.05	+0.05



**Table 3c**

Example of meteorological parameters associated to the TGF detected by AGILE on 23 April 2015 19:01:02 (UT), also presented in Tables 2a and 2b

Parameters	Values										
$t - t_{TGF}$ (min)	-40	...	-15	-10	-5	0	+5	+10	+15	...	+40
LF <sub>R</sub> (fl./5 min)	0	...	8	3	6	9	3	6	2	...	3

as stacked histograms, in order to investigate the different contributions given by the parameters under consideration.

**3.2.1. CTT**

For what concerns the cloud temperature, we obtain that most of the TGF-associated thunderstorms exhibit low values of CTT, covering a wide range of temperatures, from about  $-90$  to about  $-60$  °C, with a peak at  $\sim -77$  °C, corresponding to deep convective systems: in particular, 95% storms exhibit  $CTT < -60$  °C, with more than 23% storms showing even lower temperatures  $CTT < -80$  °C. As expected, deeper convective systems occur mostly during afternoons and over land regions, driving the general thunderstorm behavior. Most of the TGFs occurring in the western part of  $15^{\circ}W$  take place between the Atlantic Ocean and the eastern coast of Central America, following the ITCZ path, as previously shown in Figure 1: this subsample of  $\sim 30$  events is mostly associated with oceanic regions and exhibit associated storms with an average temperature  $CTT = -68$  °C. As lower latitudes imply higher tropopause and colder CTTs, convective systems with extremely low top temperatures ( $CTT < -85$  °C) are almost only observed at latitudes within  $10^{\circ}S$  and  $10^{\circ}N$ . It is interesting to notice that for latitudes within  $10^{\circ}S$  to  $10^{\circ}N$ , the CTT distribution peaks in the range  $-80$  °C  $< CTT < -70$  °C: however, 32% storms associated to AGILE TGFs (i.e., detected within the  $2.5^{\circ}S$  to  $2.5^{\circ}N$  latitude range) peak at slightly higher temperatures, in the range  $-70$  °C  $< CTT < -65$  °C.

**3.2.2. GCD**

The GCD parameter shows values peaked between  $-5$  and  $0$  °C, with a maximum at  $-2.5$  °C, as expected from mature stages of intense convection. The GCD distributions with respect to the TGF parameters generally follow what obtained for the CTT parameter, with deeper convective systems occurring during afternoons and over land, and extremely convective storms (i.e.,  $GCD < 7$  °C) taking place mainly in the  $\pm 10^{\circ}$  latitude range. Also in this case, a large fraction of AGILE TGF-associated storms exhibit slightly higher

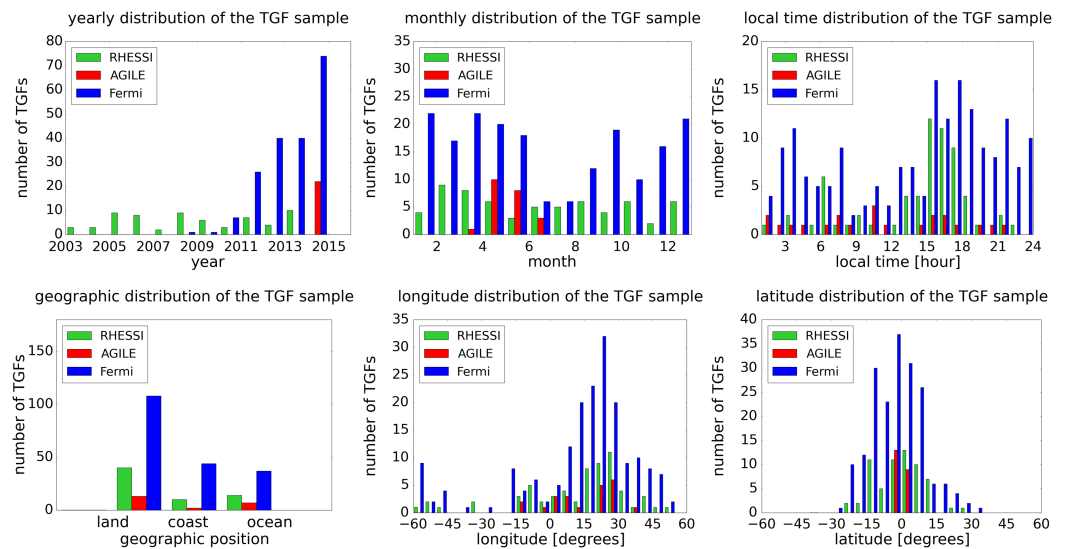


**Figure 4.** TGF properties of the population under analysis, for the RHESSI (green), AGILE (red), and Fermi (blue) subsamples, kept separated due to the different detection periods and observed regions. The first row presents the distributions with respect to year (a), month (b), and hour (c), whereas the second row shows the cumulative distributions with respect to (d) the geographic region, (e) longitude, and (f) latitude, peaking within the Tropics and mostly occurring over land regions. RHESSI = Reuven Ramaty High-Energy Spectroscopic Imager; AGILE = Astrorivelatore Gamma ad Immagini LEggero; WWLLN = World Wide Lightning Location Network; TGFs = Terrestrial Gamma ray Flashes.

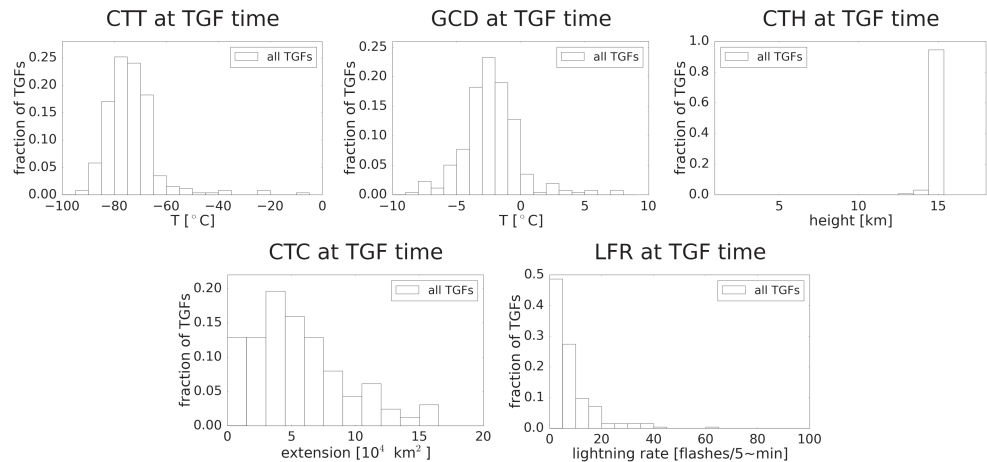


**Figure 5.** Distributions of the CTT, GCD, CTH, CTC, and LFR meteorological parameters of the TGF-associated storms. CTT = cloud top temperature; GCD = Global Convective Diagnostic; CTH = cloud top height; CTC = cloud top coverage; LFR = lightning flash rate; TGFs = Terrestrial Gamma ray Flashes.

GCD values (i.e.,  $-1\text{ }^{\circ}\text{C} < GCD < 0\text{ }^{\circ}\text{C}$ ) with respect to the other TGF-associated storms detected in the equatorial  $10^{\circ}\text{S}$  to  $10^{\circ}\text{N}$  latitude range. This shows that the usage of the GCD parameter adds very little information with respect to the use of  $10.8\text{-}\mu\text{m}$  channel temperature alone.

### 3.2.3. CTH

For what concerns the cloud top altitude, despite the CTH product has a 320-m fine vertical spatial resolution, a detailed study on cloud height is not possible, as the product is upper limited at 15,040 m, preventing any estimate on higher top clouds: as a consequence, about  $\sim 95\%$  events populate the last histogram bin of height  $\geq 15,040$  m. Nevertheless, our results confirm what obtained by Splitt et al. (2010), finding the largest fraction ( $\sim 90\%$ ) of their single-storm associated TGFs having altitudes  $> 15$  km. The 5% storms with

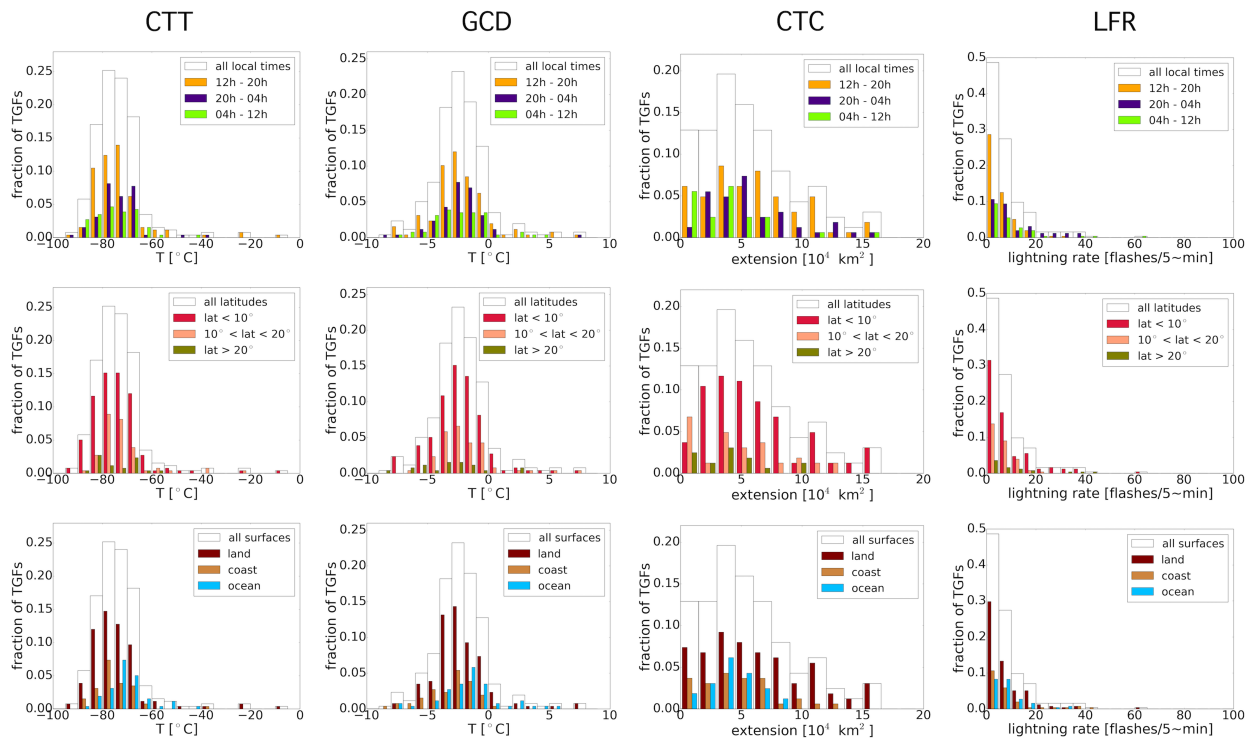


**Figure 6.** Distributions of the CTT, GCD, CTC, and LFR meteorological parameters of the TGF-associated storms for the whole TGF population evaluated with respect to the TGF parameters: local time (first row), latitude (second row), and geographic region (third row). CTT = cloud top temperature; GCD = Global Convective Diagnostic; CTH = cloud top height; CTC = cloud top coverage; LFR = lightning flash rate; TGFs = Terrestrial Gamma ray Flashes.

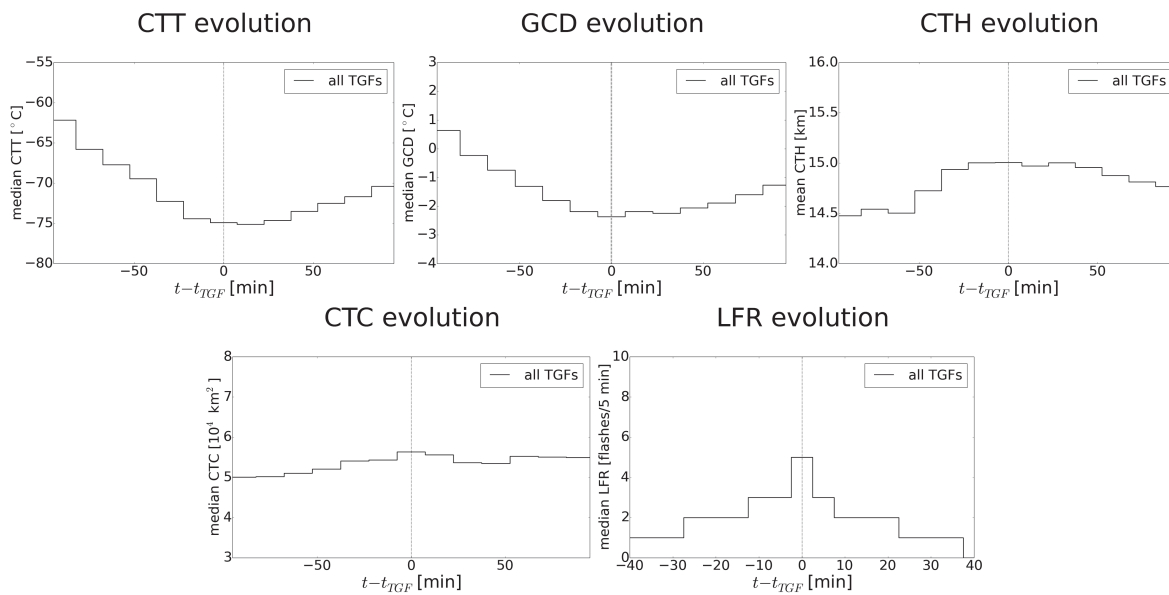


**Figure 7.** Time evolution of the CTT, GCD, CTH, CTC, and LFR meteorological parameters of the TGF-associated storms: each time step is evaluated by considering the mean value of each parameter, estimated on the whole TGF population. CTT = cloud top temperature; GCD = Global Convective Diagnostic; CTH = cloud top height; CTC = cloud top coverage; LFR = lightning flash rate; TGFs = Terrestrial Gamma ray Flashes.

$CTH < 15,040$  m include a too small number of events, to clearly characterize their behavior with respect to the TGF parameters.

### 3.2.4. CTC

The CTC distributions are characterized by a wide range of extensions, from less than 10,000 km $^2$  to more than 150,000 km $^2$ , peaking at  $CTC \sim 35,000$  km $^2$ : CTCs are quite various, as they include both single storms and large mesoscale convective systems (or at least the largest part of them), occurring within the 3.00 $^{\circ}$  radius circle considered for the analysis. The CTC distributions do not show significant variations with respect to the TGF parameters: the only clear feature regards extremely large convective systems ( $CTC > 120,000$  km $^2$ ), which seem to occur mostly during afternoons/nights, for latitudes within 10 $^{\circ}$ S to 10 $^{\circ}$ N, and over land, as expected.

### 3.2.5. LFR

Finally, the LFR distribution shows about 50% events with  $LFR < 5$  flashes per 5 min, and decreasing still exhibiting events with  $LFR > 40$  flashes per 5 min. In the  $LFR < 20$  flashes per 5-min range, the decreasing trend is generally followed by all the other subdistributions evaluated with respect to satellite, local time, latitude, and underlying regions: on the contrary, the limited number of storms with  $LFR > 20$  flashes per 5 min prevents to identify reliable preferences with respect to the TGF parameters, although they seem mostly linked to thunderstorms occurring in the night time, and within 10 $^{\circ}$ S to 10 $^{\circ}$ N latitude range.

### 3.2.6. ER and CP

For what concerns the ER and CP parameters, the 33 analyzed events exhibit quite clear behaviors. Most of the events (60%) show relatively high ER, in the 50- to 65- $\mu$ m interval, while the remaining events have lower values, between 10 and 30  $\mu$ m. All the events, except one, reach the ice phase at the cloud top.

## 3.3. TGF-Associated Storms Evolution in Time

We exploit the geostationary orbit of MSG satellites to investigate the time evolution of the convective systems associated to our TGFs, evaluating how the meteorological parameters behave in time. We took into consideration the CTT, GCD, CTH, and CTC parameters for 15-min time steps, from  $t_{TGF} - 100$  min to  $t_{TGF} + 100$  min, whereas the LFR parameter was evaluated for 5-min time steps. For the CTT, GCD, CTC, and LFR parameters, we built the time evolution trends by taking, for each time bin, the median value of each parameter, evaluated over the whole TGF data set in that time step. Using the median value, instead of the sum or the average, has the advantage of providing a central value for each parameter over the whole sample, less sensitive to outliers. On the other hand, the discrete nature of the CTH product, and the largest fraction of events with heights  $> 15,040$  m populating the last available channel of the CTH, prevents us from obtaining a reliable time profile. The CTT, GCD, CTH, and LFR parameters have been evaluated data

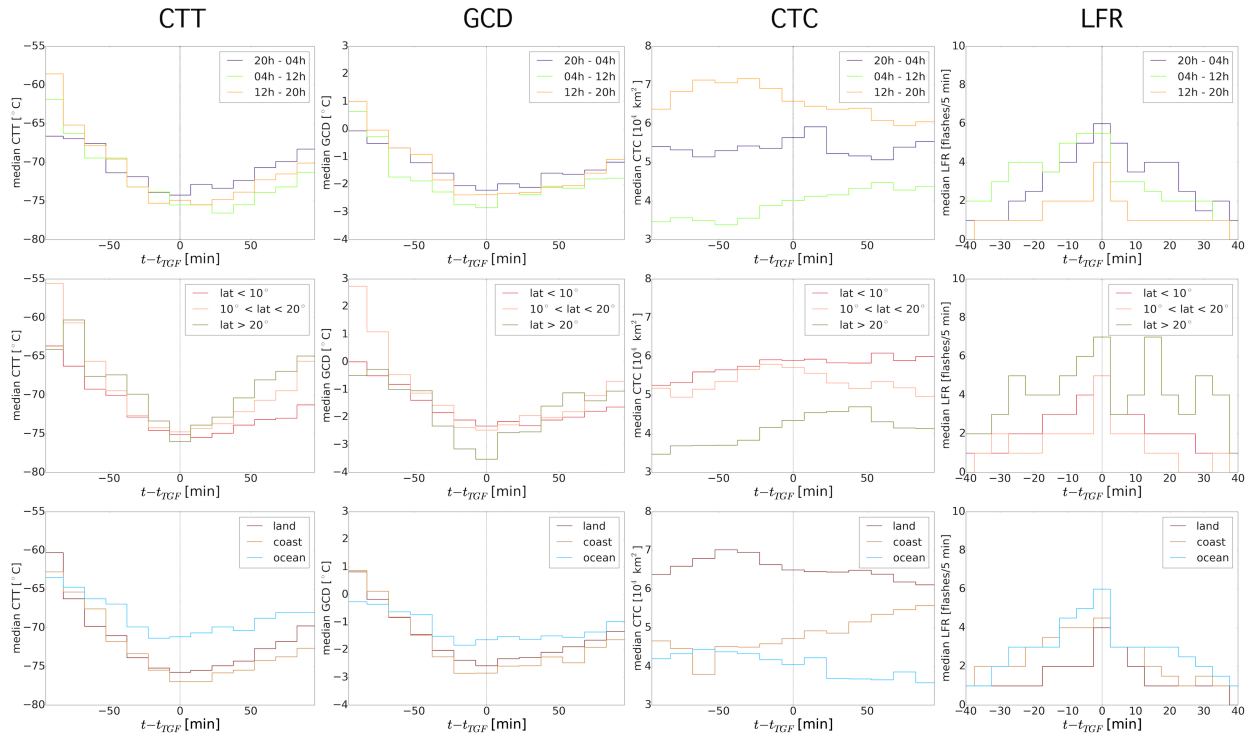


**Figure 8.** Time evolution of the CTT, GCD, CTC, and LFR meteorological parameters of the TGF-associated storms: each time step is evaluated by considering the mean value of each parameter, estimated on the whole TGF population and evaluated with respect to the TGF parameters of our sample: local time (first row), latitude (second row), and the geographic region (third row). CTT = cloud top temperature; GCD = Global Convective Diagnostic; CTH = cloud top height; CTC = cloud top coverage; LFR = lightning flash rate; TGFs = Terrestrial Gamma ray Flashes.

both within the  $0.25^\circ$  (solid line) distance around the TGF-associated spheric position; on the other hand, the CTC was evaluated in a  $3.00^\circ$  radius circle. Investigating a fixed area may result in a partial evaluation of the storm, as systems evolve and move in time. This is true especially for the CTC parameter, which is evaluated on a large  $3.00^\circ$  radius circle. However, such issues should be partially mitigated, if considering a large number of events, as in the case of our 278 TGF sample. We ended up with the distributions shown in Figures 7 and 8, whose plots are ordered as those of Figures 5 and 6.

### 3.3.1. CTT

The CTT evolution shows a clear trend that peaks (i.e., reaches its minimum value) in the  $\pm 15$ -min time window enclosing the TGF time. On average, the former cooling phase lowers the top temperature of about  $12^\circ\text{C}$  per  $100\text{ min}$  ( $CR = -0.12^\circ/\text{min}$ ), whereas the successive dissipation phase implies a warming of  $5^\circ$  per  $100\text{ min}$ , corresponding to  $+0.05^\circ/\text{min}$ , as expected from a typical thunderstorm context. This trend is generally followed by all the related distributions, expressed with respect to the TGF parameters: as already shown in Figure 5, colder top temperatures are reached for night storms, as well as for those occurring at lower latitudes  $10^\circ\text{S}$  to  $10^\circ\text{N}$  and in the coast/land regions. Events in the ocean regions exhibit rather smaller cooling rates of  $7^\circ/100\text{ min}$  ( $CR = -0.07^\circ/\text{min}$ ).

### 3.3.2. GCD

The same behavior of CTT is followed by the GCD parameter, which reaches its minimum at the TGF time as well, between a former fast cooling phase and a successive slower warming phase. As for the CTT, lower values of the GCD time evolution are reached for storms occurring in the night and over coast/land regions, in particular during the cooling phase.

### 3.3.3. CTH

As the CTH product is upper limited at  $15.04\text{ km}$ , and as each bin of these distributions is taken as the mean value of all CTH values occurring in a given 15-min time step, the final trend will be underestimated with respect to the effective altitude reached by the storm under analysis.

### 3.3.4. CTC

The CTC parameter distributions show an almost flat time profile, as each time bin represents the median CTC value of a large TGF-associated storm population, with a wide range of cloud extensions. Nevertheless,

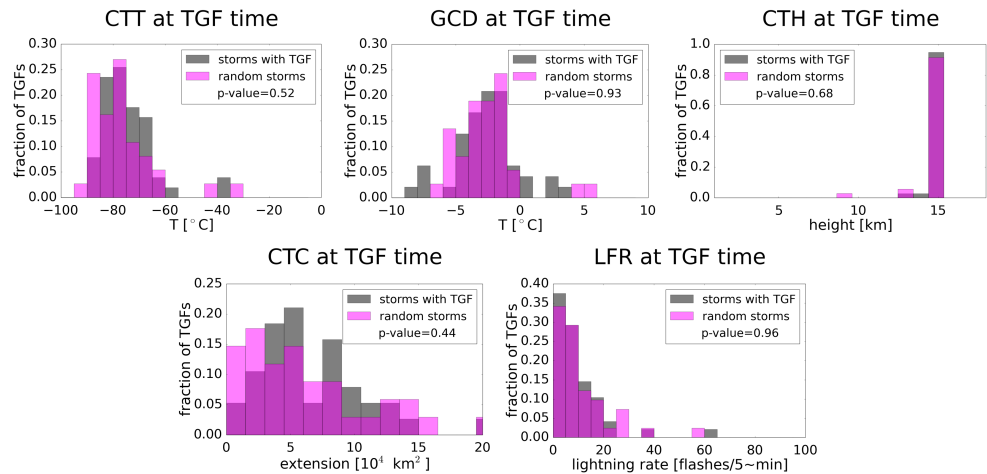


**Figure 9.** Comparison of the meteorological parameters of 50 TGF-associated storms (black) occurring over the African continent and 50 random storms (magenta) obtained by selecting random World Wide Lightning Location Network sferics taking place in the same geographic region. The distributions are evaluated at the time of the TGF/random sferic, with compatibility  $p$  values obtained by performing a Kolmogorov-Smirnov test reported in each box. CTT = cloud top temperature; GCD = Global Convective Diagnostic; CTH = cloud top height; CTC = cloud top coverage; LFR = lightning flash rate; TGFs = Terrestrial Gamma ray Flashes.

the TGF seems to take place at the end of the increasing size phase, when the median value of the CTC is  $\sim 55,000 \text{ km}^2$ . It is interesting to notice how in this case the common TGF parameters that characterize deep convection (afternoons, low latitudes, and land regions) strongly affect the associated storm average extensions, producing offset among the trends of up to  $15,000 \text{ km}^2$ . In particular, events occurring in the night time and over coast regions exhibit rather smaller average CTC values and TGFs seem not to occur at the peak time: the CTC peak seems to occur about 50 min before the afternoon TGFs, about 15 min after the night TGFs, and about 50 min after the morning TGFs.

### 3.3.5. LFR

Finally, the LFR distributions, evaluated on the  $\pm 40$ -min time intervals, all show a central peak, at  $t_{TGF} \pm 2.5$  min, where the median flash rate reaches a maximum of 5 flashes per 5 min. From a qualitative point of view, the LFR time profile with respect to local time shows that afternoon storms exhibit a larger flash rate gradient with a sharper central peak around the TGF time, whereas night storms exhibit a rather longer and more defined time structure. Quantitatively, the highest flash rate revealed for night storms could be the result of the night WWLLN detection efficiency (Hutchins et al., 2012). TGFs associated to storms occurring over the ocean show higher flash rates of six flashes per 5 min with respect to coast and land thunderstorms.

## 3.4. Cross Check With Random sferics

It is interesting to quantitatively compare the TGF-associated storms to storms for which no close TGF event was detected, in order to study the possible difference between the two populations. In order to do that, we selected a sample of random WWLLN sferics, whose associated storms can be compared to the TGF-associated ones. A remark is necessary: as the Meteosat field of view includes the largest part of the South Atlantic Anomaly, where no TGFs are detected, we cannot blindly select a sample of random sferics in the  $60^\circ\text{W}$  to  $60^\circ\text{E}$  longitude range, but we only focused on events occurring over the African continent. In order to be consistent with this choice, we also selected a subsample from our TGF sample, of events occurring within the same geographic region. We selected a subsample of 50 TGFs occurring over Africa, and compared them with a sample of 50 random storms, selected from an equal number of random WWLLN sferics, occurring within the same geographic region, between 2014 and 2017.

We carried out the same analysis performed in the previous stages of this work, by using MSG and WWLLN data, building up distributions of the meteorological parameters and the related time profiles. The distributions of the meteorological parameters for the TGF-associated and the random storms, at the TGF time, are presented in Figure 9. In order to quantitatively compare the TGF-associated and the random populations, we carried out a Kolmogorov-Smirnov (KS) test on each pair of distributions.

The CTT distributions both peak well below  $-60^{\circ}\text{C}$ , around  $CTT \sim -80^{\circ}\text{C}$  and the compatibility between the two distributions provided by the KS test is equal to a  $p$  value  $p = 52\%$ . The GCD distributions are quite similar, with both samples peaking around  $GCD \sim -2^{\circ}\text{C}$ , producing a KS  $p$  value  $p = 93\%$ . The CTH distributions, as well, exhibit very similar profiles, with almost all events occurring within cloud regions at altitudes  $CTH \geq 15,040$  m, for both populations: nevertheless, the random sample presents a fraction of events (9%) at lower altitudes, larger than in the TGF-associated one; as these two distributions are mostly characterized by a single bin, the corresponding KS test does not work properly, producing an underestimated  $p$  value equal to  $p = 68\%$ . The CTC distributions show a wide range of values up to cloud extensions  $CTC \sim 150,000$  km<sup>2</sup>: in particular, random storms exhibit about 17% more smaller size thunderstorms ( $< 20,000$  km<sup>2</sup>), with respect to TGF-associated storms, resulting in a KS  $p$  value  $p = 44\%$ . For what concerns the LFR, both distributions peak below five flashes per 5 min and decrease with a similar trend with increasing the flash rate, resulting in a KS  $p$  value of  $p = 96\%$ .

#### 4. Discussion and Conclusions

From this analysis, we obtain that storms producing TGFs are generally mostly concentrated at low latitudes, peaking in the afternoon, and mainly occurring over land regions, as expected from typical tropical thunderstorms. Nevertheless, from the point of view of those storms exhibit rather intense behaviors, characterized by very cold CTTs ( $< -75^{\circ}\text{C}$ ), high cloud top altitudes ( $> 15$  km), and large top extensions ( $> 35,000$  km<sup>2</sup>), confirming what found by Fabr o et al. (2015) for the AGILE TGFs over South America. In particular, the CTT parameter, providing information on the size of the thunderstorm, includes both single storms and large mesoscale convective systems: moreover, the LFR parameter covers flash rates from one flash per 5 min to more than 50 flashes per 5 min, characterizing storms with a wide range of intensities, from weak systems to deeper convective ones, confirming what already found by Splitt et al. (2010), regarding the cloud extension, and pointed out by Chronis et al. (2016), regarding the intensity of TGF-associated storms. An interesting information provided by the Meteosat satellites is the size of the cloud drop effective radius, that exhibit slightly large radii, peaking around 55–60  $\mu\text{m}$ , confirming the presence of deep convection in the region under analysis; moreover, the CP parameter reconstructed for each TGF-associated storm turned out to be linked to clouds with ice content.

The study of the storm evolution in time allowed to establish the preferred stage of the thunderstorm development at which TGFs more likely take place, corresponding to the peak of the cooling phase: this stage is characterized by the lowest CTT ( $\sim -75^{\circ}$ ), highest cloud top altitude ( $>15$  km), largest top extension ( $\sim 55,000$  km<sup>2</sup>), and highest flash rate ( $\sim 5$  flashes per 5 min). In particular, TGFs turn out to take place mostly within  $\pm 5$  min from the peak of the lightning activity, differently from what obtained by Smith et al. (2010).

The comparison of 50 TGF-associated thunderstorms, randomly selected within our TGF sample, with a set of 50 storms selected by choosing random WWLLN sferics from the same geographic area of our TGFs, showed that both TGF-associated and random storms exhibit quite similar distributions, with CTTs peaking at about  $-80^{\circ}\text{C}$ , maximum altitudes  $> 15.04$  km, storm extensions both covering a large range of dimensions, up to more than 150,000 km<sup>2</sup>, and LFRs mostly below five flashes per 5 min. A KS test allowed to qualitatively characterize the compatibility of the two distributions, ending up with most of the meteorological parameters exhibiting KS  $p$  values  $> 50\%$ : in particular, TGF-associated and random storms seem to be very compatible for what concerns the lightning rate ( $p$  value = 96%) and the cloud top altitude ( $p$  value = 68%), whereas the cloud extension turns out to involve larger size thunderstorms in case of TGF, resulting in a lower compatibility between the two distributions ( $p$  value = 44%). This test shows that the TGF-associated and the random storms are compatible, from the point of view of the analyzed meteorological parameters.

This work represents a pilot study on how joint analyses on TGF-associated storms can be carried out by exploiting data from the WWLLN and geostationary satellites. Future more detailed analyses should be carried out, in order to better characterize the TGF source thunderstorms. These could imply the usage of tracking algorithms, in order to follow the source region in time, instead of adopting a fixed observation area, and the usage of LEO/polar satellites, endowed with radar detectors and having a better spatial resolution. Larger and updated TGF data sets could be used, as well. Moreover, the new generation of geostationary satellites, such as the GOES-R and the Meteosat Third Generation, both endowed with an onboard lightning

imager, as well as the recently launched Atmosphere-Space Interaction Monitor, endowed with gamma ray instruments, will surely contribute to shed light on the physical properties of thunderstorms producing TGFs and on the relationship between TGFs and discharges, by performing multiwavelength observations of this puzzling phenomenon.

**Acknowledgments**

The authors wish to thank the Fermi Team and the RHESSI Team, especially Thomas Gjesteland, for the TGF data used in this paper. We also thank the World Wide Lightning Location Network (<http://wwlln.net>), for providing the lightning location data. AGILE is a mission of the Italian Space Agency (ASI), with coparticipation of INAF (Istituto Nazionale di Astrofisica) and INFN (Istituto Nazionale di Fisica Nucleare). This work was carried out in the frame of the ASI-INAFA Agreement I/028/12/0. This study was supported by the European Research Council under the European Union's 560 Seventh Framework Programme (FP7/2007-2013)/ERC Grant Agreement 320839 and the 561 Research Council of Norway under Contracts 208028/F50 and 223252/F50 (CoE). Data used for this analysis are provided as supporting information (SI) to this article. All MSG data can be downloaded from the EUMETSAT web portal (<https://eportal.eumetsat.int/>).

**References**

Abbasi, R. U., Abu-Zayyad, T., Allen, M., Barcikowski, E., Belz, J. W., Bergman, D. R., et al. (2018). Gamma ray showers observed at ground level in coincidence with downward lightning leaders. *Journal of Geophysical Research: Atmospheres*, *123*, 6864–6879. <https://doi.org/10.1029/2017JD027931>

Ackerman, S. A. (1996). Global satellite observations of negative brightness temperature differences between 11 and 6.7 micron. *Journal of Atmospheric Sciences*, *53*, 2803–2812. [https://doi.org/10.1175/1520-0469\(1996\)053<2803:GSOONB>2.0.CO;2](https://doi.org/10.1175/1520-0469(1996)053<2803:GSOONB>2.0.CO;2)

Barnes, D. E., Splitt, M. E., Dwyer, J. R., Lazarus, S., Smith, D. M., & Rassoul, H. K. (2015). A study of thunderstorm microphysical properties and lightning flash counts associated with Terrestrial Gamma-ray Flashes. *Journal of Geophysical Research: Atmospheres*, *120*, 3453–3464. <https://doi.org/10.1002/2014JD021495>

Bowers, G. S., Smith, D. M., Kelley, N. A., Martinez-McKinney, G. F., Cummer, S. A., Dwyer, J. R., et al. (2018). A Terrestrial Gamma-ray Flash inside the eyewall of Hurricane Patricia. *Journal of Geophysical Research: Atmospheres*, *123*, 4977–4987. <https://doi.org/10.1029/2017JD027771>

Bowers, G. S., Smith, D. M., Martinez-McKinney, G. F., Kamogawa, M., Cummer, S. A., Dwyer, J. R., et al. (2017). Gamma ray signatures of neutrons from a Terrestrial Gamma ray Flash. *Geophysical Research Letters*, *44*, 10,063–10,070. <https://doi.org/10.1002/2017GL075071>

Briggs, M. S., Fishman, G. J., Connaughton, V., Bhat, P. N., Paciesas, W. S., Preece, R. D., et al. (2010). First results on Terrestrial Gamma ray Flashes from the Fermi Gamma-ray Burst Monitor. *Journal of Geophysical Research*, *115*, A07323. <https://doi.org/10.1029/2009JA015242>

Briggs, M. S., Xiong, S., Connaughton, V., Tierney, D., Fitzpatrick, G., Foley, S., et al. (2013). Terrestrial Gamma-ray Flashes in the Fermi era: Improved observations and analysis methods. *Journal of Geophysical Research: Space Physics*, *118*, 3805–3830. <https://doi.org/10.1002/jgra.50205>

Carlson, B. E., Lehtinen, N. G., & Inan, U. S. (2010). Neutron production in Terrestrial Gamma ray Flashes. *Journal of Geophysical Research*, *115*, A00E19. <https://doi.org/10.1029/2009JA014696>

Celestin, S., Xu, W., & Pasko, V. P. (2012). Terrestrial Gamma ray Flashes with energies up to 100 MeV produced by nonequilibrium acceleration of electrons in lightning. *Journal of Geophysical Research*, *117*, A05315. <https://doi.org/10.1029/2012JA017535>

Chronis, T., Briggs, M. S., Priftis, G., Connaughton, V., Brundell, J., Holzworth, R., et al. (2016). Characteristics of thunderstorms that produce Terrestrial Gamma Ray Flashes. *Bulletin of the American Meteorological Society*, *97*, 639–653. <https://doi.org/10.1175/BAMS-D-14-00239.1>

Connaughton, V., Briggs, M. S., Xiong, S., Dwyer, J. R., Hutchins, M. L., Grove, J. E., et al. (2013). Radio signals from electron beams in Terrestrial Gamma ray Flashes. *Journal of Geophysical Research: Space Physics*, *118*, 2313–2320. <https://doi.org/10.1029/2012JA018288>

Cummer, S. A., Briggs, M. S., Dwyer, J. R., Xiong, S., Connaughton, V., Fishman, G. J., et al. (2014). The source altitude, electric current, and intrinsic brightness of Terrestrial Gamma ray Flashes. *Geophysical Research Letters*, *41*, 8586–8593. <https://doi.org/10.1002/2014GL062196>

Cummer, S. A., Lyu, F., Briggs, M. S., Fitzpatrick, G., Roberts, O. J., & Dwyer, J. R. (2015). Lightning leader altitude progression in Terrestrial Gamma-ray Flashes. *Geophysical Research Letters*, *42*, 7792–7798. <https://doi.org/10.1002/2015GL065228>

Dwyer, J. R. (2008). Source mechanisms of Terrestrial Gamma-ray Flashes. *Journal of Geophysical Research*, *113*, D10103. <https://doi.org/10.1029/2007JD009248>

Dwyer, J. R. (2012). The relativistic feedback discharge model of Terrestrial Gamma ray Flashes. *Journal of Geophysical Research*, *117*, A02308. <https://doi.org/10.1029/2011JA017160>

Dwyer, J. R., & Smith, D. M. (2005). A comparison between Monte Carlo simulations of runaway breakdown and Terrestrial Gamma-ray Flash observations. *Geophysical Research Letters*, *32*, L22804. <https://doi.org/10.1029/2005GL023848>

Dwyer, J. R., Smith, D. M., & Cummer, S. A. (2012). High-energy atmospheric physics: Terrestrial Gamma-ray Flashes and related phenomena. *Space Science Reviews*, *173*, 133–196. <https://doi.org/10.1007/s11214-012-9894-0>

Dwyer, J. R., Uman, M. A., Rassoul, H. K., Al-Dayeh, M., Caraway, L., Jerauld, J., et al. (2003). Energetic radiation produced during rocket-triggered lightning. *Science*, *299*, 694–697. <https://doi.org/10.1126/science.1078940>

Fabró, F., Montanyà, J., Marisaldi, M., van der Velde, O. A., & Fuschino, F. (2015). Analysis of global Terrestrial Gamma ray Flashes distribution and special focus on AGILE detections over South America. *Journal of Atmospheric and Solar-Terrestrial Physics*, *124*, 10–20. <https://doi.org/10.1016/j.jastp.2015.01.009>

Fishman, G. J., Bhat, P. N., Mallozzi, R., Horack, J. M., Koshut, T., Kouveliotou, C., et al. (1994). Discovery of intense gamma-ray flashes of atmospheric origin. *Science*, *264*, 1313–1316.

Fuschino, F., Marisaldi, M., Labanti, C., Barbiellini, G., Del Monte, E., Bulgarelli, A., et al. (2011). High spatial resolution correlation of AGILE TGFs and global lightning activity above the equatorial belt. *Geophysical Research Letters*, *38*, L14806. <https://doi.org/10.1029/2011GL047817>

Gjesteland, T., Østgaard, N., Collier, A. B., Carlson, B. E., Eyles, C., & Smith, D. M. (2012). A new method reveals more TGFs in the RHESSI data. *Geophysical Research Letters*, *39*, L05102. <https://doi.org/10.1029/2012GL050899>

Grefenstette, B. W., Smith, D. M., Hazelton, B. J., & Lopez, L. I. (2009). First RHESSI Terrestrial Gamma ray Flash catalog. *Journal of Geophysical Research*, *114*, A02314. <https://doi.org/10.1029/2008JA013721>

Gurevich, A. V., Milikh, G. M., & Roussel-Dupre, R. (1992). Runaway electron mechanism of air breakdown and preconditioning during a thunderstorm. *Physics Letters A*, *165*, 463–468. [https://doi.org/10.1016/0375-9601\(92\)90348-P](https://doi.org/10.1016/0375-9601(92)90348-P)

Hare, B. M., Uman, M. A., Dwyer, J. R., Jordan, D. M., Biggerstaff, M. I., Caicedo, J. A., et al. (2016). Ground-level observation of a Terrestrial Gamma ray Flash initiated by a triggered lightning. *Journal of Geophysical Research: Atmospheres*, *121*, 6511–6533. <https://doi.org/10.1002/2015JD024426>

Hutchins, M. L., Holzworth, R. H., Brundell, J. B., & Rodger, C. J. (2012). Relative detection efficiency of the World Wide Lightning Location Network. *Radio Science*, *47*, RS6005. <https://doi.org/10.1029/2012RS005049>

Inan, U. S., Reising, S. C., Fishman, G. J., & Horack, J. M. (1996). On the association of terrestrial gamma-ray bursts with lightning and implications for sprites. *Geophysical Research Letters*, *23*, 1017–1020. <https://doi.org/10.1029/96GL00746>

- Liu, N., & Dwyer, J. R. (2013). Modeling Terrestrial gamma Ray Flashes produced by relativistic feedback discharges. *Journal of Geophysical Research: Space Physics*, *118*, 2359–2376. <https://doi.org/10.1002/jgra.50232>
- Marisaldi, M., Argan, A., Ursi, A., Gjesteland, T., Fuschino, F., Labanti, C., et al. (2015). Enhanced detection of Terrestrial Gamma-ray Flashes by AGILE. *Geophysical Research Letters*, *42*, 9481–9487. <https://doi.org/10.1002/2015GL066100>
- Marisaldi, M., Fuschino, F., Labanti, C., Galli, M., Longo, F., Del Monte, E., et al. (2010). Detection of Terrestrial Gamma ray Flashes up to 40 MeV by the AGILE satellite. *Journal of Geophysical Research*, *115*, A00E13. <https://doi.org/10.1029/2009JA014502>
- Mecikalski, J. R., MacKenzie, W. M. Jr., Koenig, M., & Muller, S. (2010a). Cloud-top properties of growing cumulus prior to convective initiation as measured by Meteosat Second Generation. Part I: Infrared fields. *Journal of Applied Meteorology and Climatology*, *49*, 521–534. <https://doi.org/10.1175/2009JAMC2344.1>
- Mecikalski, J. R., MacKenzie, W. M. Jr., König, M., & Muller, S. (2010b). Cloud-top properties of growing cumulus prior to convective initiation as measured by Meteosat Second Generation. Part II: Use of visible reflectance. *Journal of Applied Meteorology and Climatology*, *49*, 2544–2558. <https://doi.org/10.1175/2010JAMC2480.1>
- Mezentsev, A., Østgaard, N., Gjesteland, T., Albrechtsen, K., Lehtinen, N., Marisaldi, M., et al. (2016). Radio emissions from double RHESSI TGFs. *Journal of Geophysical Research: Atmospheres*, *121*, 8006–8022. <https://doi.org/10.1002/2016JD025111>
- Mosher, F. R. (2001). A satellite diagnostic of global convection.
- Moss, G. D., Pasko, V. P., Liu, N., & Veronis, G. (2006). Monte Carlo model for analysis of thermal runaway electrons in streamer tips in transient luminous events and streamer zones of lightning leaders. *Journal of Geophysical Research*, *111*, A02307. <https://doi.org/10.1029/2005JA011350>
- Pasko, V. P. (2014). Electrostatic modeling of intracloud stepped leader electric fields and mechanisms of Terrestrial Gamma ray Flashes. *Geophysical Research Letters*, *41*, 179–185. <https://doi.org/10.1002/2013GL058983>
- Roberts, O. J., Fitzpatrick, G., Priftis, G., Bedka, K., Chronis, T., McBreen, S., et al. (2017). Terrestrial Gamma ray Flashes due to particle acceleration in tropical storm systems. *Journal of Geophysical Research: Atmospheres*, *122*, 3374–3395. <https://doi.org/10.1002/2016JD025799>
- Roberts, O. J., Fitzpatrick, G., Stanbro, M., McBreen, S., Briggs, M. S., Holzworth, R. H., et al. (2018). The first Fermi-GBM Terrestrial Gamma ray Flash catalog. *Journal of Geophysical Research: Space Physics*, *123*, 4381–4401. <https://doi.org/10.1029/2017JA024837>
- Rodger, C. J., Brundell, J. B., Holzworth, R. H., & Lay, E. H. (2009). Growing detection efficiency of the World Wide Lightning Location Network. In *American Institute of Physics Conference Series*, American Institute of Physics Conference Series, *1118*, pp. 15–20. <https://doi.org/10.1063/1.3137706>
- Schmetz, J., Pili, P., Tjemkes, S., Just, D., Kerkmann, J., Rota, S., & Ratier, A. (2002). An introduction to Meteosat Second Generation (MSG). *Bulletin of the American Meteorological Society*, *83*, 977–992. [https://doi.org/10.1175/1520-0477\(2002\)083<0977:AITMSG>2.3.CO;2](https://doi.org/10.1175/1520-0477(2002)083<0977:AITMSG>2.3.CO;2)
- Shao, X.-M., Hamlin, T., & Smith, D. M. (2010). A closer examination of Terrestrial Gamma-ray Flash-related lightning processes. *Journal of Geophysical Research*, *115*, A00E30. <https://doi.org/10.1029/2009JA014835>
- Smith, D. M., Dwyer, J. R., Hazelton, B. J., Grefenstette, B. W., Martinez-McKinney, G. F. M., Zhang, Z. Y., et al. (2011). A Terrestrial Gamma ray Flash observed from an aircraft. *Journal of Geophysical Research*, *116*, D20124. <https://doi.org/10.1029/2011JD016252>
- Smith, D. M., Hazelton, B. J., Grefenstette, B. W., Dwyer, J. R., Holzworth, R. H., & Lay, E. H. (2010). Terrestrial Gamma ray Flashes correlated to storm phase and tropopause height. *Journal of Geophysical Research*, *115*, A00E49. <https://doi.org/10.1029/2009JA014853>
- Smith, D. M., Lopez, L. I., Lin, R. P., & Barrington-Leigh, C. P. (2005). Terrestrial Gamma-ray Flashes observed up to 20 MeV. *Science*, *307*, 1085–1088.
- Splitt, M. E., Lazarus, S. M., Barnes, D., Dwyer, J. R., Rassoul, H. K., Smith, D. M., et al. (2010). Thunderstorm characteristics associated with RHESSI identified Terrestrial Gamma ray Flashes. *Journal of Geophysical Research*, *115*, A00E38. <https://doi.org/10.1029/2009JA014622>
- Tran, M. D., Rakov, V. A., Mallick, S., Dwyer, J. R., Nag, A., & Heckman, S. (2015). A Terrestrial Gamma-ray Flash recorded at the Lightning Observatory in Gainesville, Florida. *Journal of Atmospheric and Solar-Terrestrial Physics*, *136*, 86–93. <https://doi.org/10.1016/j.jastp.2015.10.010>
- Ursi, A., Guidorzi, C., Marisaldi, M., Sarria, D., & Frontera, F. (2017). Terrestrial Gamma-ray Flashes in the BeppoSAX data archive. *Journal of Atmospheric and Solar-Terrestrial Physics*, *156*, 50–56. <https://doi.org/10.1016/j.jastp.2017.02.014>
- Ursi, A., Sanò, P., Casella, D., Marisaldi, M., Dietrich, S., & Tavani, M. (2017). A pipeline to link meteorological information and TGFs detected by AGILE. *Journal of Geophysical Research: Space Physics*, *122*, 2300–2309. <https://doi.org/10.1002/2016JA023137>
- Wilson, C. T. R. (1924). The electric field of a thundercloud and some of its effects. *Proceedings of the Physical Society of London*, *37*, 32D–37D.
- Wilson, C. T. R. (1925). The acceleration of  $\beta$ -particles in strong electric fields such as those of thunderclouds. *Proceedings of the Cambridge Philosophical Society*, *22*, 534. <https://doi.org/10.1017/S0305004100003236>
- Xu, W., Celestin, S., & Pasko, V. P. (2012). Source altitudes of Terrestrial Gamma-ray Flashes produced by lightning leaders. *Geophysical Research Letters*, *39*, L08801. <https://doi.org/10.1029/2012GL051311>